Electrochimica Acta 100 (2013) 118–124

Contents lists available at SciVerse ScienceDirect

Electrochimica Acta

journal homepage: www.elsevier.com/locate/electacta

The activation/depassivation of nickel–chromium–molybdenum alloys in bicarbonate solution: Part I

A.K. Mishra [a], S. Ramamurthy [b], M. Biesinger [b], D.W. Shoesmith [a,b,*]

[a] Department of Chemistry, University of Western Ontario, London, ON, N6A 5B7 Canada
[b] Surface Science Western, 999 Collip Circle, London, ON, N6G 0J3 Canada

ARTICLE INFO

Article history:
Received 14 February 2013
Received in revised form 28 March 2013
Accepted 28 March 2013
Available online 6 April 2013

Keywords:
Nickel–chromium–molybdenum alloys
Hybrid-BC1 alloy
Bicarbonate
XPS
AES

ABSTRACT

Electrochemical and surface analytical techniques (X-ray photoelectron and Auger spectroscopies) were used to characterize the influence of potential on the properties of the oxide film formed on the Hybrid BC-1 (a Ni–Cr–Mo) alloy in chloride solutions containing bicarbonate. In the passive region the film possesses the expected bilayer structure with a Cr(III)-dominated barrier layer containing mixed oxidation states of Mo and an outer dominantly-hydroxide layer. At more positive potentials the Cr/Mo content of the film decreases when bicarbonate is present and the alloy becomes covered by a thick (>100 nm), and only partially protective, $Ni(OH)_2$ layer

1. Introduction

Nickel–Chromium–Molybdenum alloys are widely used in corrosion resistant applications. They owe their exceptional corrosion resistance to a thin protective oxide (passive) film, which protects the underlying metal/alloy [1]. The major alloying elements, chromium (Cr) and molybdenum (Mo), play an important role in maintaining the passivity of the alloy, Cr primarily by forming a passive barrier oxide layer on the surface, while Mo is thought to inhibit localized corrosion by repairing the barrier layer after breakdown [2–5]. Efforts to optimize the Cr and Mo contents resulted in significant improvements in the corrosion resistance in aggressive environments [6]. This last decade has seen a considerable effort focused on understanding the corrosion behavior of these highly corrosion resistant Ni–Cr–Mo alloys in aggressive environments, since C-22 (UNS N06022) (Ni–22Cr–13Mo–3W) was chosen as a candidate material for nuclear waste containers in the Yucca Mountain project (Nevada, USA).

Many recent studies on Ni–Cr–Mo or Ni–Cr–Mo–W alloys have concentrated on low pH conditions, either in bulk acidic solution [4,6–9] or under crevice corrosion conditions [5,10–17] when a low pH environment can exist beneath the crevice former. Lloyd et al. [6] studied the effect of major alloying elements, Cr, Mo and W on the passive film behavior of various Ni–Cr–Mo (W) alloys in acidic solution. Based on electrochemical and surface analytical studies, it was reported that the high-Cr alloys developed better passive oxide films due to their higher Cr content and the increased segregation of Cr–Ni to the inner oxide and Mo–W to the outer oxide.

Recently, Zhang et al. [18] investigated the influence of pH and temperature on passive film stability on the C-2000 alloy (UNS N06200) (Ni–23Cr–16Mo–1.6Cu). Based on X-ray photoelectron spectroscopy (XPS) and time of flight-secondary ion mass spectroscopy (TOF-SIMS) analyses they showed that an increase in Ni, and decreases in Cr and Mo, contents occurred when the temperature was increased from 50 °C to 90 °C. While this would be expected to destabilize the passive film it was offset by an increase in thickness of both the inner barrier layer oxide and the outer hydroxide layer. The influence of pH was studied using the same surface analytical techniques. As the pH decreased (from 7 to 4 to 1) the film thickness decreased, but this was compensated by an increase in the Cr and Mo contents of the film. These results are consistent with those of Lloyd et al. [6,19] and explain why the passivity is maintained down to at least pH = 1. However, a more detailed XPS analysis showed that, despite this increase in Cr content, there was a relative decrease in the overall Cr (III) oxide content of the barrier layer at the alloy/oxide interface, a clear sign that the film would eventually destabilize when the pH was decreased further.

* Corresponding author at: Department of Chemistry, University of Western Ontario, London, ON, N6A 5B7 Canada. Tel.: +1 519 661 2111x86366.
E-mail addresses: dwshoesm@uwo.ca, ajitosu@gmail.com (D.W. Shoesmith).

0013-4686/$ – see front matter © 2013 Elsevier Ltd. All rights reserved.
http://dx.doi.org/10.1016/j.electacta.2013.03.161

In room temperature solutions, Zhang et al. have demonstrated [18,20] that excellent passivity is maintained up to 200 mV (vs SCE) for both C-22 and C-2000 even in extremely concentrated chloride (5.0 mol/L) solution. However, potentiodynamic studies on C-22 in a concentrated simulated groundwater (SCW), containing chloride, nitrate, sulphate, fluoride, bicarbonate/carbonate (pH 9.7; 95 °C), showed the presence of an anodic peak at ~250 mV (SCE) [21]. This peak was present only when carbonate/bicarbonate was present in the solution. Additionally, if the potential was held potentiostatically in this region, and a sufficient load applied, the C-22 alloy experienced transgranular corrosion and failed by SCC. By contrast, when carbonate/bicarbonate was absent only plastic deformation was observed despite the presence of a high chloride concentration [21,22].

Dunn et al. [23] characterized the electrochemically grown oxide film on C-22 at different potentials in this solution (SCW) as well as in solutions containing either chloride (0.19 mol/L) or bicarbonate (1.14 mol/L). In the chloride solution the film thickness at a potential of 400 mV (SCE) was only ~30–40 nm. By contrast in bicarbonate solution and SCW the film thickness at this potential, within the anodic peak region, was ~200 nm and ~300 nm, respectively. The oxide film thickness was determined by the depth at which the Ni concentration reached a constant value, which would lead to an over estimation of oxide film thickness which is best determined as the depth at which the oxygen concentration reaches half of its maximum value [24–26]. It was proposed that Cr depletion in bicarbonate and SCW was the cause of SCC in this potential region [21].

Szmodis et al. [27] characterized the oxide film formed on C-22 in SCW solution at 90° C using XPS and atomic force microscopy (AFM). The XPS spectra of an oxide film grown at a potential in the anodic peak region (~200–400 mV, SSC) contained Ni peak, but no peaks for Cr, Mo and W. Further, the AFM studies showed that the oxide film was porous with interconnected filaments. Most recently, Zadorozne et al. [28] observed this anodic peak in bicarbonate solutions for C-22 alloy, Alloy 800H (Ni–21Cr–45Fe) and Alloy 600 (Ni–16Cr–9Fe) but not for Alloy 201 (Ni–0.1Fe), the only alloy not containing Cr as an alloying element. The authors also observed that the anodic peak potential decreases with increase in temperature. However, no discussion of the origin of the peak was discussed.

These studies show that an enhanced anodic current in this potential region is generally observed for Cr-containing Ni-based alloys in bicarbonate/carbonate solutions, and may be a precursor to SCC. To date no convincing explanation of this behavior has been offered. In this paper a more comprehensive electrochemical and surface analytical study of this phenomenon is presented using the Hybrid-BC1 (UNS N10362) (Ni–15Cr–22Mo) alloy.

2. Experimental

2.1. Electrode and solution preparation

A cubic specimen of Hybrid-BC1 alloy with a total surface area of 14.06 cm^2 was cut from plate material supplied by Haynes International, Kokomo, Indiana (USA). A small tapped hole was machined on the top of the specimen to enable contact to a cylindrical rod. This connector to the external circuit was sheathed in glass and sealed with a Teflon gasket to prevent contact with the electrolyte. The specimen (working electrode) was then polished with a series of wet silicon carbide papers up to 1200 grit, rinsed with deionized water and acetone, and then air dried prior to an electrochemical experiment. The specimen was partially immersed in the electrolyte to avoid the possibility of a crevice site at the Teflon/specimen interface. A platinum foil and a saturated calomel electrode (SCE) were used as the counter and reference electrodes, respectively.

A standard jacketed, three-electrode cell was connected to a water circulating thermostatic bath allowing control of the solution temperature to within 1 °C. The reference and counter electrodes were housed in separate compartments attached to the main body of the glass cell through glass frits. The cell was placed in a Faraday cage to reduce external sources of electrical noise. The solution was deaerated with Ar throughout the experiment. Experiments were conducted in 1 M NaCl, 0.1 M $NaHCO_3$, and 1 M NaCl + 0.1 M $NaHCO_3$ solutions at 60 °C. The pH of the solution used was recorded before and after each experiment. The solution was prepared using deionized (DI) Milli-Q Millipore water (18.2 MΩ cm) and reagent grade salts. A fresh solution was prepared for each experiment and all experiments were repeated at least twice to confirm reproducibility.

2.2. Electrochemical methods

The corrosion potential (E_{corr}) was recorded for 1 h before each polarization experiment. Potentiodynamic scans were performed from ~250 mV below E_{corr} to 800 mV at a scan rate of 0.167 mV/s. Oxide films for surface analyses were grown by scanning the potential from E_{corr} to the desired film growth potential and then holding it there for 9 h. A slow scan from E_{corr} to the applied potential was used instead of the commonly applied potential step. This avoided the initial surge in current which is always observed when a potential step is applied. No cathodic cleaning was performed before any electrochemical experiment.

Previous studies on Ni alloys show that the cyclic potentiodynamic polarization (CPP) technique is not a conservative approach for determining susceptibilities to localized corrosion [10,14]. Consequently, the potentiodynamic–potentiostatic–potentiodynamic (PD–PS–PD) technique was used. The potential was scanned at 0.167 mV/s from ~250 mV below E_{corr} to different potentials above the apparent film breakdown potential, held at a potential for 9 h and then scanned back to E_{corr}. The absence of positive hysteresis in the current–potential curve is an indication that no localized corrosion initiated.

2.3. Surface characterization techniques

Electrodes anodically oxidized for surface analyses were rinsed gently with DI water and air dried prior to characterization. SEM images were obtained on a Hitachi S-4500 field emission SEM equipped with an EDAX™ EDX system at Surface Science Western (SSW). XPS analyses were performed with a Kratos AXIS Nova XPS at SSW employing monochromatic Al K_α (1486.7 eV) radiation. The binding energy was calibrated to give an Au $4f_{7/2}$ line position at 83.95 eV. XPS spectra were corrected for charging by taking the C 1s spectrum for adventitious C to be at a binding energy of 284.8 eV. Survey spectra were recorded on all samples followed by high resolution XPS spectra for the Ni 2p, Cr 2p, Mo 3d, C 1s and O 1s regions. The XPS spectra were analyzed using the commercial CasaXPS™ software.

Auger analyses were performed using a PHI 660 Auger electron spectrometer (AES) instrument with an excitation energy of 5 keV. Depth profiles were obtained by sputtering using an Ar^+ ion beam. A survey scan was acquired for each sample and during depth profiling the signal intensities for Ni, Cr, Mo and O were monitored as a function of sputtering time. To convert sputtering times to depths, similar measurements were performed on a Hybrid-BC1 alloy

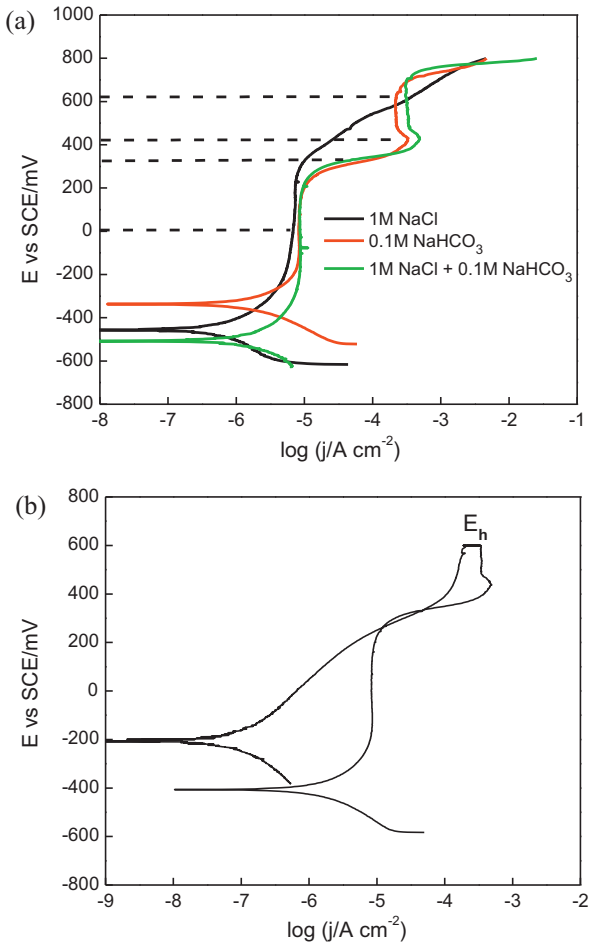

Fig. 1. (a) Potentiodynamic curve for the Hybrid-BC1 alloy recorded in 1 M NaCl, 0.1 M. $NaHCO_3$ and 1 M NaCl + 0.1 M $NaHCO_3$ solutions at 60 °C. The dashed lines indicated. The potentials used in experiments to produce XPS and Auger specimens and (b) a PD–PS–PD curve in 1 M NaCl + 0.1 M $NaHCO_3$ solution at 60 °C.

covered with an air-formed native oxide. The sputtering rate obtained on this reference specimen was 28 nm/min and it was assumed that the sputtering rate for an electrochemically oxidized surface was similar to that of the reference specimen.

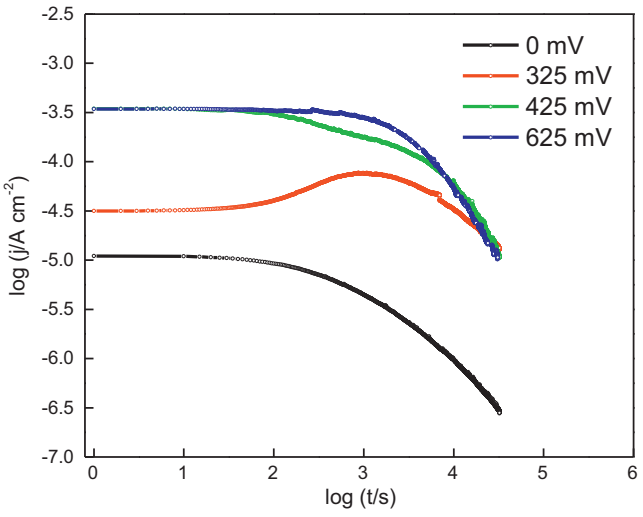

Fig. 2. Current–time plots recorded on the Hybrid-BC1 alloy in 1 M NaCl + 0.1 M $NaHCO_3$ at. 60 °C.

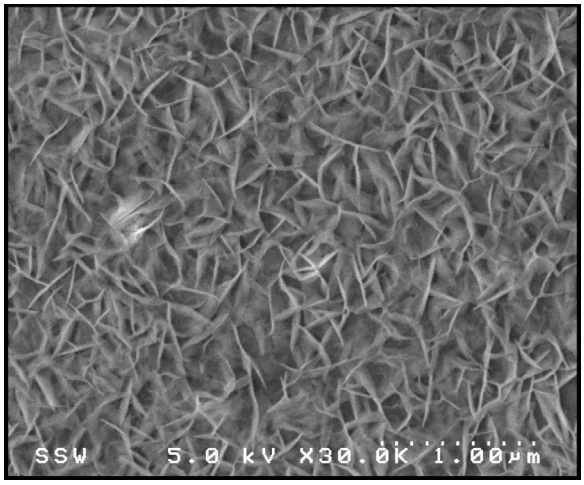

Fig. 3. SEM micrograph of the oxide film grown at 425 mV in the chloride/bicarbonate solution at 60 °C.

3. Results and discussion

3.1. Electrochemical film growth

Fig. 1(a) shows the potentiodynamic curve recorded on the Hybrid-BC1 alloy in chloride, bicarbonate and chloride/bicarbonate

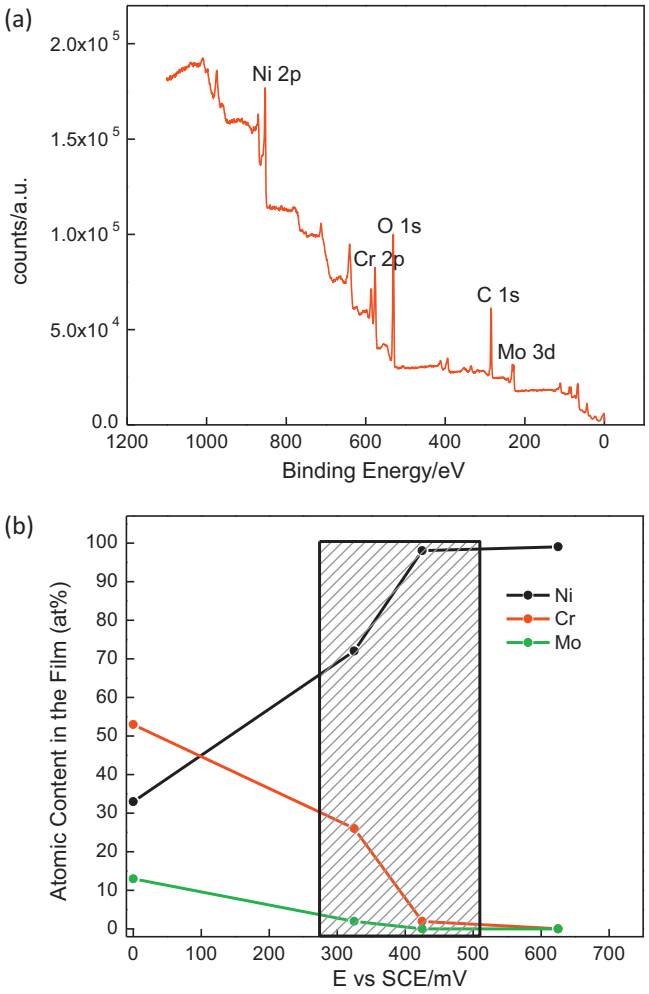

Fig. 4. (a) Survey spectrum recorded on the Hybrid-BC1 alloy at 0 mV in chloride/bicarbonate solution at 60 °C and (b) film cation composition (normalized) determined from XPS survey spectra. The shaded region shows the potential range containing the anodic current peak.

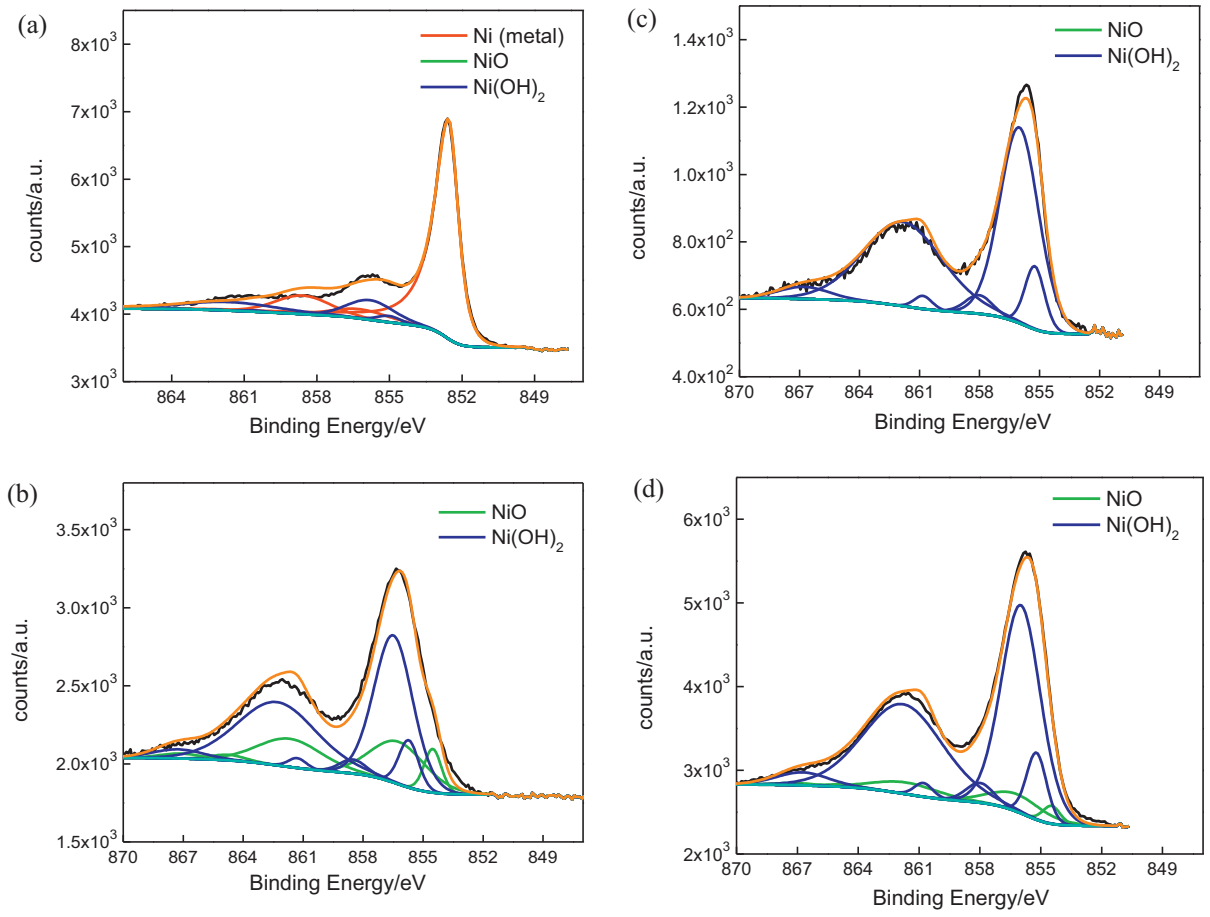

Fig. 5. Deconvoluted high resolution XPS spectrums for the Ni 2p region recorded on a film grown at (a) 0 mV, (b) 325 mV, (c) 425 mV, and (d) 625 mV in chloride/bicarbonate solution at 60 °C.

solutions at 60 °C. The pH of the chloride solution changed from 7.3 to 6.8 during the course of the experiment. In the case of the bicarbonate and chloride/bicarbonate solution, the pH of the solution remained effectively constant at 8.3. At higher potentials, an anodic peak is observed at ~400 mV (SCE) in both the bicarbonate and chloride/bicarbonate solutions but not in the chloride-only solution. At potentials beyond this peak pseudo-passive behavior is observed in the potential range, ~450–750 mV. These results demonstrate that the state of the electrode surface after the barrier layer degradation at potentials >~200 mV is different to that in the chloride solution. The rapid increase in the current beyond 200 mV in the bicarbonate-containing solution could result in localized corrosion.

To determine whether this is the case the PD–PS–PD technique was applied. The potential was scanned to 600 mV, held potentiostatically for 9 h and then scanned back to a potential lower than E_{corr}. As shown in Fig. 1(b), no positive hysteresis indicating the onset of localized corrosion was observed. Similar experiments were performed at a series of potentials (E_h) throughout the range from 200 mV to 600 mV, but did not reveal a positive hysteresis, confirming that the current increase at potentials >200 mV is not due to the onset of localized corrosion but to a general degradation of the surface oxide.

To characterize the surface composition, oxide films were grown potentiostatically at potentials of 0, 325, 425 and 625 mV; i.e., before, around and beyond the anodic peak, as indicated by the dashed lines in Fig. 1(a). Fig. 2 shows the current at all four potentials plotted on a log–log scale. The early independence of current on time can be attributed to the modification of the native oxide initially present during the potentiodynamic scan to E_h. The eventual logarithmic decay in current can then be attributed to the further growth, compositional change and the defect annealing of the surface oxide.

In the passive region (0 mV) the current decays to a very low value consistent with the formation of a passive layer. At 325 mV (i.e., in the rising current region prior to the peak potential, Fig. 1(a)) the initial current is higher than at 0 mV, as expected, but then increases before finally decaying again. The current increase indicates an initial degradation in the film properties before the degraded film begins to improve again. At the two highest applied potentials this transient behavior is not observed, the degradation process in the film probably having occurred during the potentiodynamic scan through the anodic peak region. Eventually, the current at long times becomes independent of potential for $E \geq 325$ mV, suggesting the properties of the film are identical. Since steady-state has not been achieved after 9 h of potentiostatic oxidation, the pseudo-passive properties of the film continue to improve.

3.2. Surface analyses

3.2.1. SEM results

The film grown at 0 mV is featureless and the original surface roughness remains visible as expected for the formation of a very thin passive film only a few nanometers thick. The SEM image in Fig. 3 shows the film grown at 425 mV (the peak potential) is porous, at least superficially, consistent with the higher current observed. However, the continuing decrease in current with time, Fig. 2(b), indicated that this film is becoming more resistive with time,

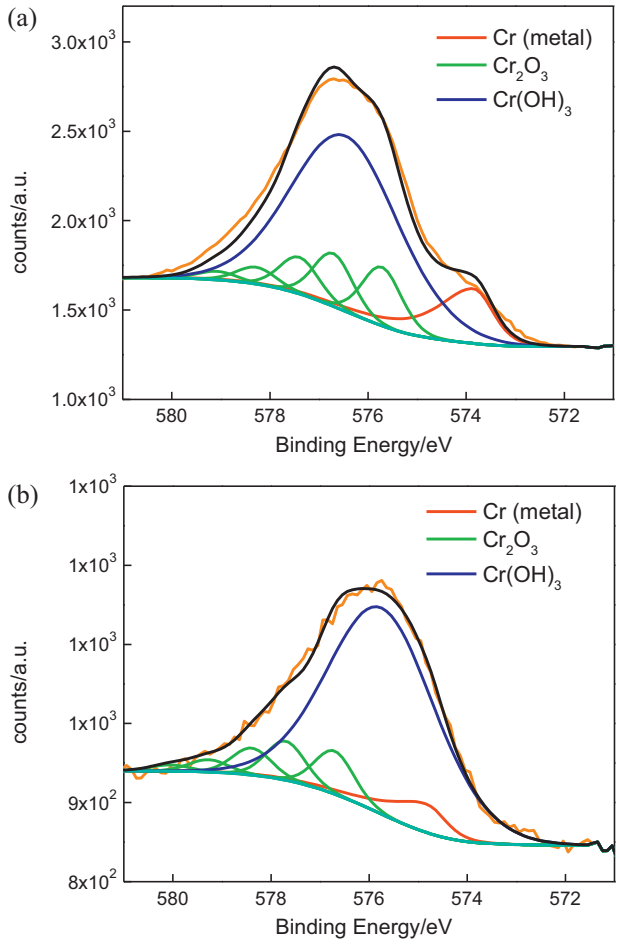

Fig. 6. Deconvoluted high resolution XPS spectrum for the Cr 2p region recorded on a film grown at (a) 0 mV and (b) 325 mV in chloride/bicarbonate solution at 60 °C.

possibly due to a resealing (at least partially) of the pores shown in Fig. 3.

3.2.2. XPS results

XPS survey spectra were recorded at all four potentials: the spectrum for 0 mV recorded in the chloride/bicarbonate solution is shown in Fig. 4(a) as an example and contains the Ni 2p, Cr 2p, Mo 3d, O 1s and C 1s peaks. The normalized cation composition (Ni, Cr and Mo) of the oxide film, corrected for any contribution from the alloy substrate (determined from high resolution spectra) is plotted as a function of applied potential in Fig. 4(b). The shaded area in this figure indicates the potential region containing the current peak. In the passive region (0 mV), the film was found to be composed of ~50% Cr, ~30% Ni and ~10% Mo. As expected, the passive film is enriched in Cr. When the potential is increased to 325 mV, a potential in the rising section of the anodic peak (Fig. 1(a)), the concentration of Ni in the oxide film increased significantly at the expense of Cr and Mo. In the anodic peak region and above, the film was completely transformed to Ni oxide/hydroxide, with little to no Cr and Mo. These analyses confirm the formation of a non-protective film, as suggested by the SEM image in Fig. 3, which is predominantly Ni oxide/hydroxide and apparently completely depleted in Cr and Mo.

Fitted high-resolution XPS spectra, recorded for the Ni 2p, Cr 2p, Mo 3d, O 1s and C1s regions are shown, corrected using a Shirley background correction, in Figs. 5–7. The spectra were deconvoluted for the different contributing species according to the procedures

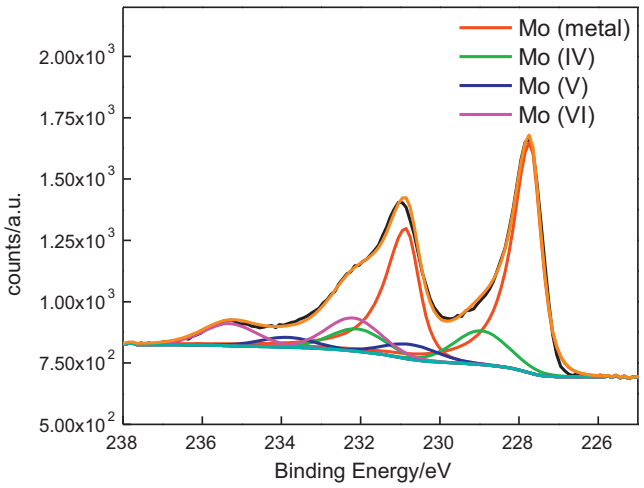

Fig. 7. Deconvoluted high resolution XPS spectra for the Mo 3d region recorded on a film grown at 0 mV in chloride/bicarbonate solution at 60 °C.

published by Biesinger et al. [29,30], Biesinger et al. [30,31], and McIntyre et al. [32] for Ni, Cr, and Mo, respectively.

For all elements a signal for metal is only observed after anodic film growth in the passive region (0 mV). At this potential for Ni, $Ni(OH)_2$ is the dominant species detected in the film, Fig. 5. For Cr a substantial contribution from Cr^{III} oxide is observed, Fig. 6(a), the relative contributions of Cr species being 12%, 26%, and 64% for Cr(metal), Cr_2O_3 and $Cr(OH)_3$, respectively. For Mo the percentages for Mo(IV), Mo(V), and Mo(VI) are 14%, 6% and 14%, respectively, Fig. 7. These percentages are consistent with expectations for a passive film on Ni–Cr–Mo alloys based on previous analyses for the C-22 and C-2000 alloys [18,20]. The high Cr_2O_3 content is consistent with the presence of a passive barrier layer and the mixed oxidation states of Mo and high hydroxide contents for both Ni and Cr with the presence of an outer hydroxide layer.

On increasing the anodic potential the film thickness increases and the signals for metallic species are no longer observed, Fig. 4(b). For Ni, the spectrum is dominated by the oxide/hydroxide content, Fig. 5(b), while for Cr the Cr_2O_3 content is substantially reduced, the relative proportions of Cr_2O_3 and $Cr(OH)_3$ being 14% and 83% (the remaining 3% being Cr(metal)). For Mo, no signal is detected, indicating the presence of a film thick enough to obscure the substrate alloy with a degraded barrier layer covered by an oxide/hydroxide film containing no Mo.

Further increasing the potential to 425 mV (i.e., to approximately the anodic peak potential value, Fig. 4(b)) yields a film which is dominantly $Ni(OH)_2$. The apparently complete absence of Cr and Mo in the film, Fig. 4(b), suggests the protective Cr-containing barrier layer is effectively destroyed and the protective segregated outer layer of Mo oxide/hydroxide lost. This conversion to $Ni(OH)_2$ with increasing potential is clearly demonstrated in Fig. 8 which shows the at% of the various Ni species detected in the film at all four potentials. The shaded area shows the potential range of the anodic peak. The residual predominantly $Ni(OH)_2$ surface film is porous, Fig. 3, and partially protective as indicated by the higher currents observed, Fig. 1(a) and 2(b). Depending on the thickness of the film it is possible that the thick outer layer of $Ni(OH)_2$/NiO obscures a sublayer containing Cr and Mo at the alloy/oxide interface but undetectable by XPS. Since the current after 9 h at the three higher potentials continues to decrease with time the alloy surface is becoming more protected either by the thickening of the partially protective $Ni(OH)_2$ layer or by the regrowth of a partially protective barrier layer at the alloy/oxide interface.

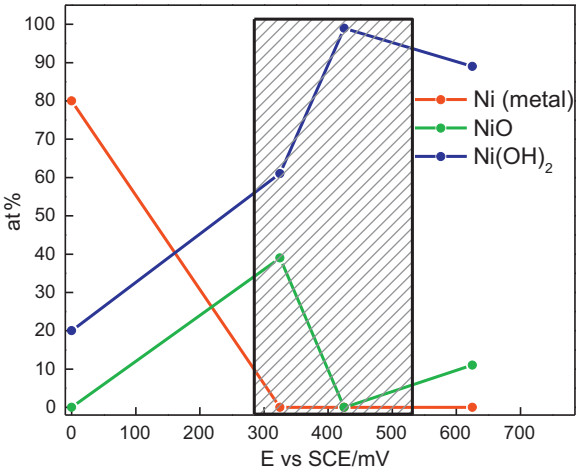

Fig. 8. Atomic concentrations of Ni species obtained from deconvolution of high resolution XPS spectra as a function of applied potential after oxidation in chloride/bicarbonate solution at 60 °C. The shaded region shows the potential range containing the anodic peak.

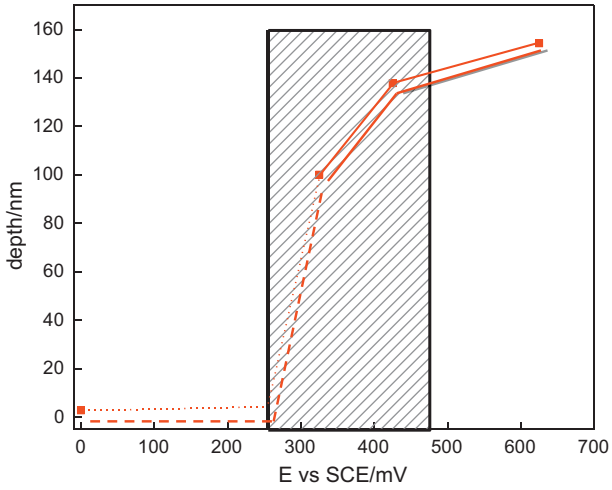

Fig. 10. Film thickness as a function of applied potential for films grown in chloride/bicarbonate solution at 60 °C. The shaded region shows the potential range containing the anodic peak potential.

3.2.3. AES analyses

AES analyses were performed to determine the variation in film composition with depth and the film thickness as a function of applied potential. The films analyzed were anodically grown using the same potential scan and 9 hour potentiostatic hold employed in the XPS experiments. The depth profiles recorded at the four potentials are shown in Fig. 9 and the film thicknesses in Fig. 10. Oxide thicknesses were obtained from these profiles as the sputtering depth at which the O signal reached half of its maximum (surface) value. The shaded region in the figure shows the potential range from barrier layer degradation to just beyond the peak current.

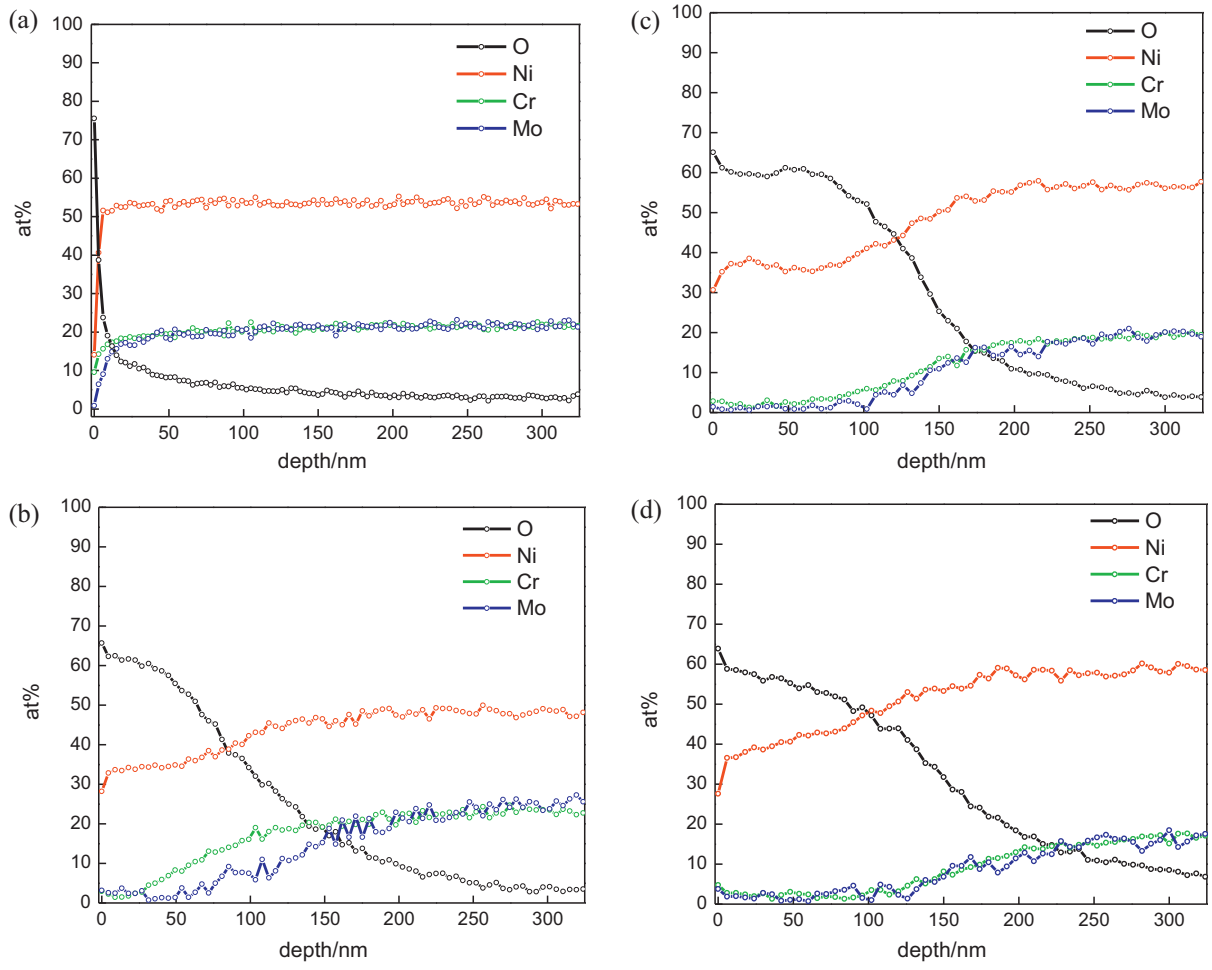

Fig. 9. AES depth profiles measured on film grown at (a) 0 mV, (b) 325 mV, (c) 425 mV, and (d) 625 mV in chloride/bicarbonate solution at 60 °C.

These profiles confirm the presence of a thin film in the passive region (0 mV) and a major increase in film thickness once the current increases into the anodic peak region. The profile recorded after oxidation at 325 mV confirms the XPS results showing that at this potential (after 9 h) the film retains some Cr in the inner regions of the film at the film/alloy interface while Mo is considerably more depleted. At the highest two potentials the film is depleted throughout of Cr and Mo. These results confirm that the decreasing currents in Fig. 2 can be attributed to the thickening of the $Ni(OH)_2$ film and that no residual or regrown Cr/Mo-containing barrier layer is present at the alloy surface.

4. Conclusions

Potentiodynamic polarization curves recorded on the Hybrid BC-1 Ni–Cr–Mo alloy show an unexpected increase in anodic current at potentials at which passivity is maintained in the absence of carbonate. Experiments using the PD–PS–PD technique show that this is due to a general degradation in film properties not the onset of localized corrosion.

XPS analyses confirm that, at lower potentials, prior to the current increase, the surface is covered by a thin oxide with high Cr(III) oxide content and containing mixed Mo oxidation states as expected in a passive film.

XPS analyses also show that the current increase is accompanied by the loss of Cr and Mo leading to a film which is effectively $Ni(OH)_2$ containing small amounts of NiO.

Auger spectroscopy measurements confirm these chemical changes and demonstrate that the $Ni(OH)_2$ film is up to two orders of magnitude thicker than the passive film and only partially protective to the substrate alloy.

Acknowledgements

This research was funded by the Canadian Natural Sciences and Engineering Research Council (NSERC). The author also acknowledges Haynes International for providing the samples.

References

[1] W.Z. Friend, Corrosion of Nickel and Nickel-Based Alloys, John Wiley and Sons, NY, 1980.
[2] M. Moriya, M.B. Ives, The structure of anodic films formed on nickel and nickel—13 w/o molybdenum alloy in pH 2.8 sodium sulfate solution, Corrosion 40 (1984) 62.
[3] R.S. Lillard, M.P. Jurinski, J.R. Scully, Crevice corrosion of alloy 625 in chlorinated ASTM artificial ocean water, Corrosion 50 (1994) 251.
[4] J.R. Hayes, J.J. Gray, A.W. Szmodis, C.A. Orme, Influence of chromium and molybdenum on the corrosion of nickel-based alloys, Corrosion 62 (2006) 491.
[5] P. Jakupi, F. Wang, J.J. Noel, D.W. Shoesmith, Corrosion product analysis on crevice corroded alloy-22 specimens, Corrosion Science 53 (2011) 1670.
[6] A.C. Lloyd, J.J. Noel, N.S. McIntyre, D.W. Shoesmith, Cr, Mo and W alloying additions in Ni and their effect on passivity, Electrochimica Acta 49 (2004) 3015.
[7] A.C. Lloyd, J.J. Noel, N.S. McIntyre, D.W. Shoesmith, The open circuit ennoblement of alloy C-22 and other Ni–Cr–Mo alloys, JOM 57 (2005) 31.
[8] J.J. Gray, J.R. Hayes, G.E. Gdowski, B.E. Viani, C.A. Orme, Influence of solution pH, anion concentration, and temperature on the corrosion properties of alloy 22, Journal of Electrochemical Society 153 (2006) B61.
[9] M.A. Rodriguez, R.M. Carranza, R.B. Rebak, Passivation, Depassivation of Alloy 22 in acidic chloride solutions, Journal of Electrochemical Society 157 (2010) C1.
[10] A.K. Mishra, G.S. Frankel, Crevice corrosion repassivation of alloy 22 in aggressive environments, Corrosion 64 (2008) 836.
[11] P. Jakupi, J.J. Noel, D.W. Shoesmith, Crevice corrosion initiation and propagation on alloy-22 under galvanically-coupled and galvanostatic conditions, Corrosion Science 53 (2011) 3122.
[12] B.A. Kehler, G.O. Illevbare, J.R. Scully, Crevice corrosion stabilization and repassivation behavior of alloy 625 and alloy 22, Corrosion 57 (2001) 1042.
[13] X. Shan, J.H. Payer, Characterization of the corrosion products of crevice corroded alloy 22, Journal of Electrochemical Society 156 (2009) C313.
[14] K.J. Evans, A. Yilmaz, S.D. Day, L.L. Wong, J.C. Estill, R.B. Rebak, Using electrochemical methods to determine alloy 22s crevice corrosion repassivation potential, JOM 57 (2005) 56.
[15] N.S. Zadorozne, C.M. Giordano, M.A. Rodriguez, R.M. Carranza, R.B. Rebak, Crevice corrosion kinetics of nickel alloys bearing chromium and molybdenum, Electrochimica Acta 76 (2012) 94.
[16] M.A. Rodriguez, Inhibition of localized corrosion in chromium containing stainless alloys, Corrosion Reviews 30 (2012) 19.
[17] M.R. Ortiz, M.A. Rodriguez, R.M. Carranza, R.B. Rebak, Determination of the crevice corrosion stabilization and repassivation potentials of a corrosion-resistant alloy, Corrosion 66 (2010) 1.
[18] X. Zhang, D. Zagidulin, D.W. Shoesmith, Characterization of film properties on the Ni–Cr–Mo alloy C-2000, Electrochimica Acta 89 (2013) 814.
[19] A.C. Lloyd, D.W. Shoesmith, N.S. McIntyre, J.J. Noel, Effects of temperature and potential on the passive corrosion properties of alloy C22 and C276, Journal of Electrochemical Society 150 (2003) B120.
[20] D. Zagidulin, X., Zhang, J., Zhou, J.J., Noel, D.W. Shoesmith, Characterization of surface composition on alloy 22 in neutral chloride solutions, Surface and Interface Analysis. http://dx.doi.org/10.1002/sia.5204
[21] K.T. Chiang, D.S. Dunn, G.A. Cragnolino, Effect of simulated groundwater chemistry on stress corrosion cracking of alloy 22, Corrosion 63 (2007) 940.
[22] K.J. King, L.L. Wong, J.C. Estill, R.B. Rebak, Slow Strain Rate Testing of Alloy 22 in Simulated Concentrated Ground Waters, Corrosion, Paper No. 04548, NACE, New Orleans, LA, March 28–April 1, 2004.
[23] D.S. Dunn, Y.M. Pan, K.T. Chiang, G.A. Cragnolino, Surface Analysis of Alloy 22 Under Conditions that Promote Stress Corrosion Cracking, Corrosion, Paper No. 06509, NACE, San Diego, CA, March 12–16, 2006.
[24] A.S. Lim, A. Atrens, ESCA studies of Ni–Cr alloys, Applied Physics A: Solids and Surfaces 54 (1992) 343.
[25] S. Mischler, A. Vogel, H.J. Mathieu, D. Landolt, The chemical composition of the passive film on Fe–24Cr and Fe–24Cr–11Mo studied by AES, XPS and SIMS, Corrosion Science 32 (1991) 925.
[26] M.G. Faichuk, S. Ramamurthy, W.M. Lau, Electrochemical behaviour of alloy 600 tubing in thiosulphate solution, Corrosion Science 53 (2011) 1383.
[27] A.W. Szmodis, K.L. Anderson, J.C. Farmer, T. Lian, C.A. Orme, Environmental Influence on Passive Films Formed on Alloy 22 (UNS N06022), Corrosion, Paper No. 03692, San Diego, CA, March 16–20, 2003.
[28] N.S. Zadorozne, R.M. Carranza, M.C. Giordano, A.E. Ares, R.B. Rebak, Effect of Temperature and Chloride Concentration on the Anodic Behavior of Nickel Alloys in Bicarbonate Solutions, Corrosion, Paper No. 0001413, Salt Lake City, UT, March 11–15, 2012.
[29] M.C. Biesinger, B.P. Payne, L.W.M. Lau, A.R. Gerson, R.S. Smart, X-ray photoelectron spectroscopic chemical state quantification of mixed nickel metal, oxide and hydroxide systems, Surface and Interface Analysis 41 (2009) 324.
[30] M.C. Biesinger, B.P. Payne, A.P. Grosvenor, L.W.M. Lau, A.R. Gerson, R.S. Smart, Resolving surface chemical states in XPS analysis of first row transition metals, oxides and hydroxides: Cr, Mn, Fe, Co and Ni, Applied Surface Science 257 (2011) 2717.
[31] M.C. Biesinger, C. Brown, J.R. Mycroft, R.D. Davidson, N.S. McIntyre, X-ray photoelectron spectroscopy studies of chromium compounds, Surface and Interface Analysis 36 (2004) 1550.
[32] P.A. Spevac, N.S. McIntyre, Thermal reduction of molybdenum trioxide, Journal of Physical Chemistry 96 (1992) 9029.